

# AFFORDABLE STABILITY IN HEIGHT MEASUREMENT

In a proof-of-concept study, Hittech Multin successfully designed and built a cost-efficient level sensor, specifically aimed at semiconductor applications, using mostly off-the-shelf parts and a self-developed processing algorithm. The target measurement stability was 50 nm. Experiments on a 300-mm wafer showed a short-term instability between 6.4 nm and 10<sup>2</sup> nm, at the centre and the edge of the measurement range, respectively. The next research stage will focus on bringing stability performance within specification throughout the entire range. Finally, the sensor's ability to also measure wafer tilt (Rx and Ry), for counteracting tilt-dependent wafer height measurement errors, will be investigated.

THOMAS OOMS AND FRED COUWELEERS

## Technical introduction

The most critical step in the fabrication of a computer chip is lithography. In this step, the pattern of the electric circuits is 'written' on a wafer. A lithography system essentially projects an (electron-) optical image onto a resist-coated wafer. (Note: exposure using either photons (light) or electron beams is possible.) The top surface of the wafer must be in the (electron-) optical focal plane throughout the exposure or else the written pattern will be blurred, which would result in a non-functioning chip. The axial range in which the image is sharp is called the depth-of-focus (*DOF*), which can be calculated using the expression:

$$DOF = \lambda / (2 \cdot NA^2)$$

Here,  $\lambda$  is the wavelength of the light used and  $NA$  is the numerical aperture at the image side of the (electron-) optical system [1]. Lithography systems of the deep-UV generation use light with a wavelength near 200 nm. To write patterns as small as possible, these systems have an  $NA$  as large as 1 [-]. The *DOF* is then approximately 100 nm.

Capacitive sensors are available commercially that have a resolution as small as a few nanometers [2]. It is therefore possible to measure and (with proper actuation) control the wafer height with sufficient precision. However, to avoid a volume conflict with the (electron-) optical column, these sensors must be outside this column. The height measurements done at those locations only lead to the correct height at the centre of the column when the wafer is sufficiently flat. An optical sensor can measure on the (electron-) optical axis. A sensing light beam can travel at an angle towards the (nominal) intersection of (electron-) optical axis and wafer top-surface, reflect and then travel to a detector at the other side of a level-sensor (LS) module (Figure 1).

We decided to include the development of a "Level Sensor for application in Semiconductor Industry" in our internal technology development programme. The aim was to design and build an optical level sensor based on low-coherence interferometry, using standard parts, that is capable of measuring wafer height changes of 50 nm (resolution), over a vertical range of 300  $\mu$ m (peak-to-peak). It turned out that deriving the wafer height from the optical sensor signals (signal processing) is not a trivial task in the presence of noise and changes in signal shape related to wafer height.

## AUTHORS' NOTE

Thomas Ooms holds a Ph.D. degree in Applied Physics (2008) from Delft University of Technology (NL).

He has worked at Mapper Lithography and Hittech Multin, and currently works at ASML. His expertise is in the design of (optical) metrology solutions to accomplish accurate positioning in high-tech systems.

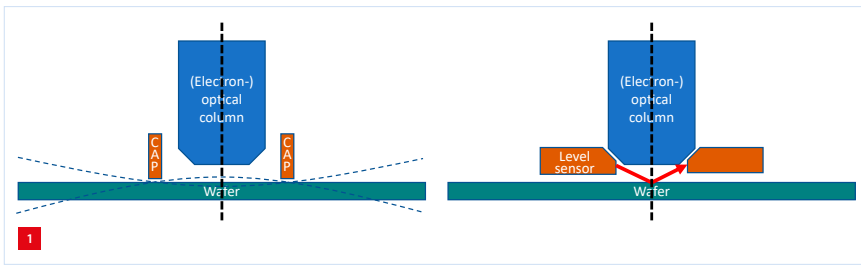
Fred Couweleers holds a Master's degree in Applied Physics (1990) from Eindhoven University of Technology (NL). He has worked predominantly in the field of (optical) metrology in industry and contract research organisations with a focus on production. Currently, he works as a senior optical designer at Hittech Multin on various optics projects, including microscopy, beam shaping and data merging.

fcouweleers@hittech.com

## Hittech Group

Hittech Multin, located in Den Haag (NL), is part of the Hittech Group, which comprises nine companies in the Netherlands, Germany and Malaysia, and has a turnover of €140 million. Hittech is a first-tier system supplier in mechatronic and optical systems, and is active in the semicon, medical and lab equipment markets. The development group at Hittech Multin was responsible for the design and realisation of the level sensor within the framework of the "Sensors for Semicon" part of Hittech's Technology Program, under the supervision of Pieter Kappelhof, director Technology of the Hittech Group.

PKAPPELHOF@HITTECH.COM  
WWW.HITTECH.COM



Off-axis measurement using capacitive sensors (left) versus on-axis measurement by an optical sensor (right).

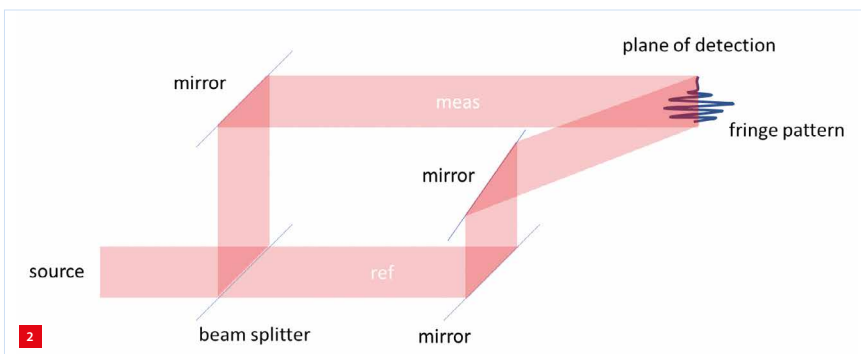
### Concept design

To reach the required resolution, the sensor technology was based on interferometry. A single optical power measurement (one measurement using one photo-detector) is insufficient to generate a reliable height measurement, e.g. because the single power measurement would depend on the unknown wafer reflectivity. Instead, it is necessary to record a pattern with multiple fringes. This is realised by varying optical path length (OPL) within the interferometer.

The OPL can be varied as a function of time, for example by a scanning mirror in the reference branch. But the OPL can also be varied as a function of space, for example by letting the two interferometer beams combine at an angle onto a pixel-array sensor (camera) in a Mach Zehnder-like design (Figure 2). The second option was chosen so as to minimise the number of parts required and avoid having to generate small, but very reproducible, movements.

Although the typical light source for interferometry is a laser, such a highly coherent light source would result in a signal that is periodic over a large wafer-height range. In this case, it would be impossible to redetermine the wafer height after the measurement beam has been interrupted, for example during a wafer swap, because there is no way to tell how many fringes the signal has shifted after interruption with respect to the signal before interruption. To avoid this ambiguity, the sensor uses a low-coherent light source.

As the light source has low coherence, the fringe pattern will only appear where the OPL of the two interferometer beams



Layout of a Mach Zehnder-like interferometer.

is almost equal, as shown in Figure 3. When the wafer is at the bottom of its range, the measurement beam wavefront arrives 'late' at the detector, compared to the corresponding reference beam wavefront. The fringe pattern then forms near one edge of the detector. When the wafer is at the centre of its range, the fringe pattern forms at the centre of the detector. When the wafer is at the top of its range, the fringes form near the other side of the detector. See Figure 3.

The essence of data processing is to determine the position of the fringes on the detector. The wafer height  $Z_{waf}$  can then be estimated by multiplying this position with a proportionality factor.

### Detailed design

#### Hardware

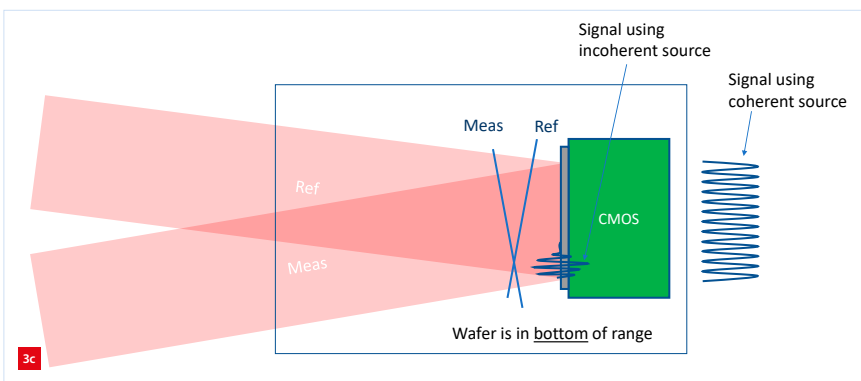
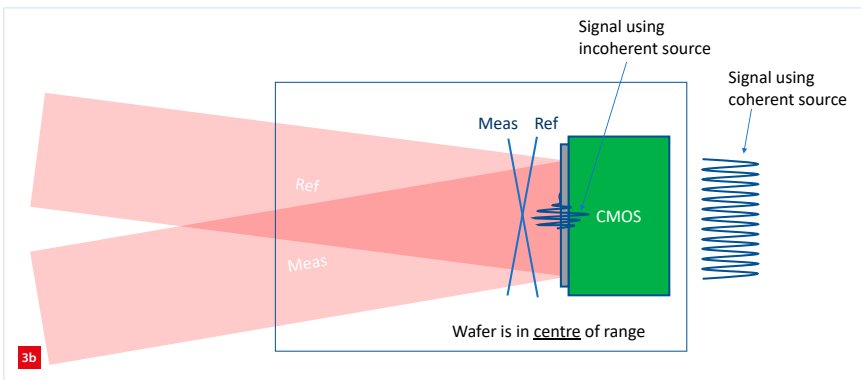
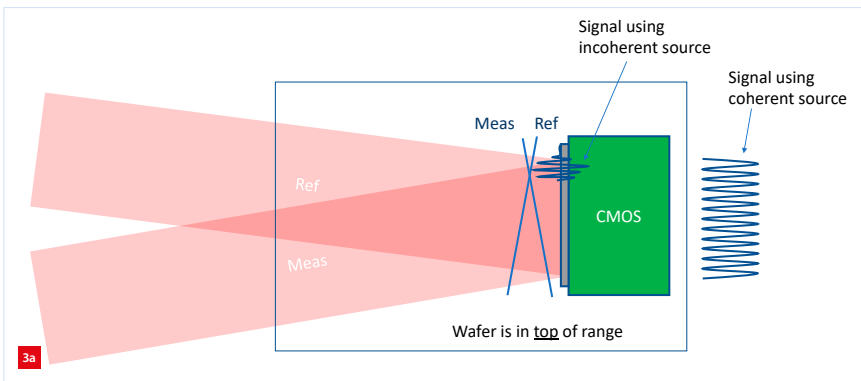
After the measurement concept had been validated in a breadboard set-up, the detailed design of the LS prototype commenced. The LS prototype was designed to consist of two modules, an 'electronics box' and a 'ring'. The ambition was to use commercial off-the-shelf parts, apart from a custom part to position the optomechanical parts with respect to each other and to serve as an interface to the environment (e.g. the lithography tool).

The electronics box contains a low-coherent infrared light source (super luminescent diode, SLD [3]), which emits light through a polarisation-maintaining (PM) single-mode (SM) fibre. An 840 nm wavelength was chosen because the SLD with this wavelength has a particularly large bandwidth, which leads to a narrow interference pattern (i.e., with relatively few fringes; an OPL difference of 5.3 wavelengths reduces the fringe contrast by only 50%), which reduces the chance of making a height measurement error due to an OPL measurement error of one or more exact wavelengths. A laptop PC performs real-time data analysis and displays the results.

The ring receives light via a PM SM fibre. Inside the ring body, light is collimated and split into a measurement branch and a reference branch. Light in the measurement branch travels (via mirrors) to the wafer (angle of incidence AOI with respect to the normal is 68°), reflects and travels to a 'primary interference plane'. This large angle of incidence is derived from the volume claim in an earlier project and provides ample space for an (electron-) optical column in the centre of the ring. The change in OPL as a result of a change in wafer height is:

$$dOPL = 2 \cdot dZ \cdot \cos(AOI)$$

In this geometry, the result is:  $dOPL = 0.75 \cdot dZ$ .

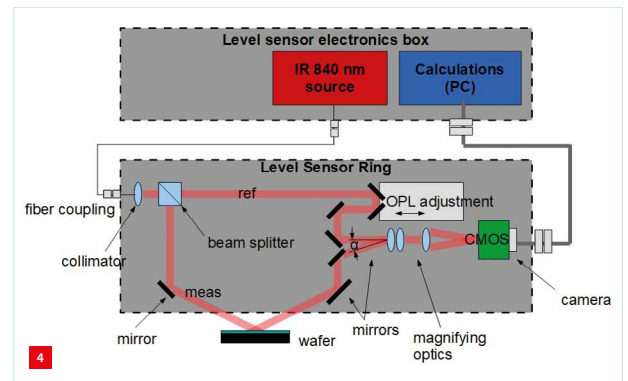


The effect of wafer height on the fringe pattern on the sensor for a coherent and an incoherent source.

The reference beam travels via mirrors to the same interference plane. The *OPL* of the two branches must differ by less than a few  $\mu\text{m}$ . In this prototype, a sufficiently small difference in *OPL* between the reference and measurement beam cannot be accomplished by the stacking of manufacturing tolerances, so a mechanical *OPL*-adjustment was added in the reference beam (Figure 4). This is used for a one-time adjustment to be executed during sensor production.

A compromise had to be found between ensuring that the sensor is able to resolve the interference pattern and ensuring that the measurement range requirement is met. If two beams of light with wavelength  $\lambda$  arrive at a plane under angles  $+\alpha/2$  and  $-\alpha/2$ , respectively, the period in the interference pattern in that plane,  $p$ , is given by:

$$p = \lambda / (2 \cdot \sin(\alpha/2))$$

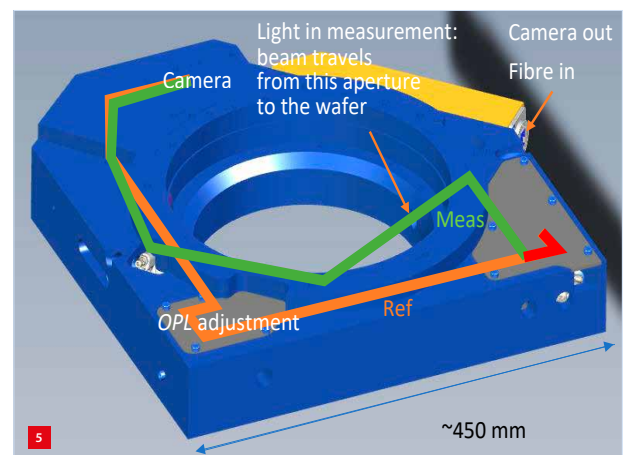


The level sensor consisting of two modules: the electronics box and the ring.

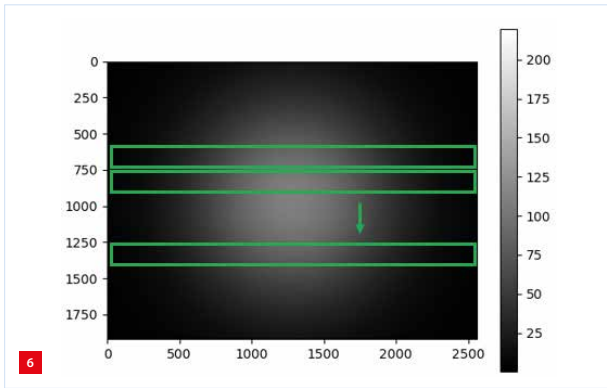
We do not account for the facts that we need to see the complete fringe pattern, the *OPL* matching is not perfect, and there is a wafer placement error with respect to the 'zero' position. Then, in first order, the wafer height measurement range is the sensor size multiplied by a proportionality factor between *OPL* and wafer height, divided by the period in the interference pattern. A small angle  $\alpha$  will give a large period, which is easy to resolve but will give a small measurement range, while a large angle  $\alpha$  will give a small period in the interference pattern, which is difficult to resolve but will give a large measurement range.

The values for the different parameters describing the design are listed below:

- Angle between beams in primary interference plane  $\alpha = 16^\circ \rightarrow$  period  $p = 3.0 \mu\text{m}$ .
- Magnifying optics magnification  $M = 2.5 [-] \rightarrow$  period on camera  $p = 7.5 \mu\text{m}$ .
- Camera has  $N_x = 2,560$  pixels with distance  $d_{\text{pix}} = 2.2 \mu\text{m}$  [4]  $\rightarrow$  size of camera = 5.6 mm; one fringe is 3.4 pixels (in compliance with the Shannon-Nyquist sampling criterion: to be able to fully reconstruct a signal, it must be sampled at a rate at least twice the highest (spatial) signal frequency [5]); measurement range is



Sensor ring: the central part is empty to provide volume for an (electron-) optical column.



A simulated image of the irradiance of two interfering spots on the CMOS sensor. The xy-axes of the figure represent the xy-position on the CMOS-sensor in pixels. The scale bar is 8-bit intensity. One data set (green box) contains ten pixel rows. Forty of these sets are used per recorded frame.

$((5,600/7.5) - 2 \cdot 3 \cdot 5.3) \cdot 0.84 - 10 - 50 = 540 \mu\text{m}$  in terms of OPL  $\rightarrow$  according to the equation ( $dOPL = 0.75 \cdot dZ$ ) derived previously, the range is  $720 \mu\text{m}$  in terms of wafer height.

- Beam diameter = 3.3 mm.

A 3D model of the sensor ring is shown in Figure 5 (path of reference and measurement beams indicated by orange and green lines, respectively).

#### Processing algorithm

The essence of data processing is to determine the position of the fringes. This position is converted to an estimated wafer height by multiplication using a proportionality factor. More specifically, the data processing determines the displacement of fringes with respect to a 'zero measurement'. So, the sensor actually measures a wafer height change ( $dZ_{\text{waf}}$ ) between a zero measurement and an actual measurement. The steps of the data-processing algorithm are described below.

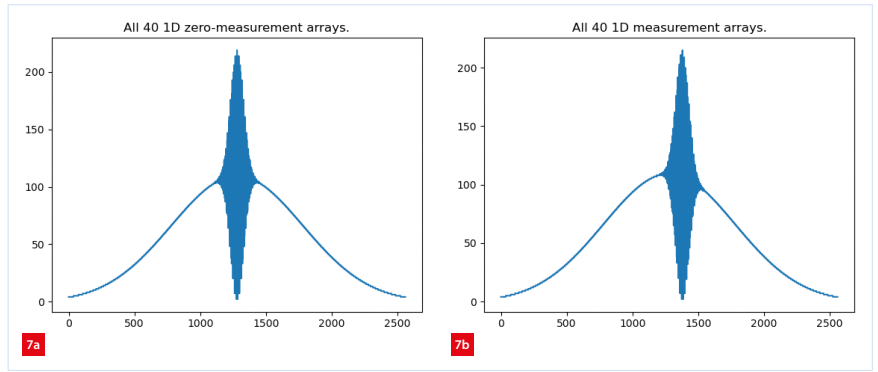
For every frame, forty sets of ten rows (of 2,560 pixels each) are evaluated (Figure 6) – not all pixel rows are used.

Within each set, the average over the ten rows is determined, to suppress noise. The result is 40 1D irradiance arrays (as function of  $x$ ) per recorded frame. We arrived at these numbers by trial and error, compromising between noise suppression and contrast loss.

According to theory, the recorded irradiance distribution at any point on the detector,  $I_{\text{tot}}$ , which is actually  $I_{\text{tot}}(x, y)$ , can be expressed as:

$$I_{\text{tot}} = I_{\text{meas}} + I_{\text{ref}} + 2 \sqrt{I_{\text{meas}} \cdot I_{\text{ref}}} \cdot \cos(\phi_{\text{meas}} - \phi_{\text{ref}}) \cdot \Gamma(\phi_{\text{meas}} - \phi_{\text{ref}})$$

Here,  $I_{\text{meas}}$  and  $I_{\text{ref}}$  are the irradiance of the measurement and reference beam, respectively, while  $\phi_{\text{meas}}$  and  $\phi_{\text{ref}}$  are the phases of these two beams, respectively, (leading to an interference term) and  $\Gamma$  is a function that expresses



Two simulated examples of recorded irradiance. The horizontal axis represents x-position on the CMOS-sensor, as unit pixels. The vertical axis represents irradiance, normalised to a scale 0-255 [-].

- (a) Zero measurement.  
(b) Actual measurement.

light source coherence as a function of phase difference (reducing the interference term as the phase difference increases). Two theoretical examples of  $I_{\text{tot}}$  are presented in Figure 7, showing simulated image intensity along a pixel row for two different wafer heights.

The two graphs in Figure 7 show that – for different wafer heights resulting in different fringe positions – the shape of the fringe pattern is different (the left side of Figure 7 is horizontally symmetrical, while the right side is not). The fringe pattern is modulated by the position-dependent  $I_{\text{meas}}$  and  $I_{\text{ref}}$ . This shape change hinders the data-processing task of determining the fringe pattern displacement. The solution is to include a normalisation step, which removes the shape change. The result is a normalised irradiance  $I_{\text{norm}}$ :

$$I_{\text{norm}} = \frac{I_{\text{tot}} - (I_{\text{meas}} + I_{\text{ref}})}{2 \sqrt{I_{\text{meas}} \cdot I_{\text{ref}}}}$$

After this step, the fringe pattern will (theoretically) be as shown in Figure 8.

The next data-processing step truly determines the fringe pattern shift (position difference between zero measurement and actual measurement). Consider the normalised irradiance of the zero measurement,  $I_{\text{zero}}(x)$ , and the actual measurement,  $I_{\text{act}}(x)$ . They have the following Fourier transforms:

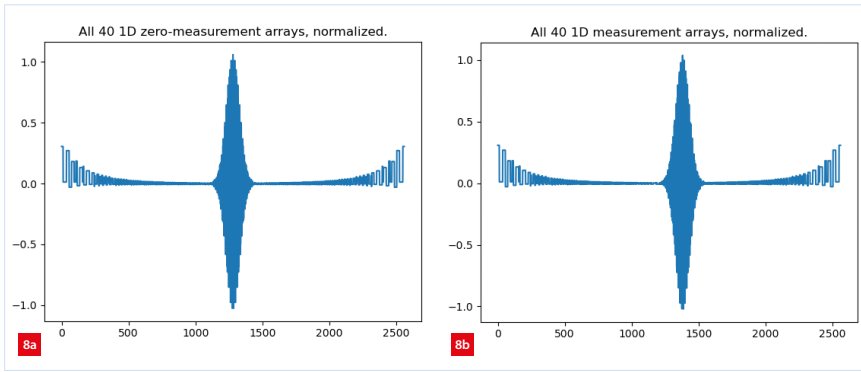
$$\text{FT}(I_{\text{zero}}(x)) = J_{\text{zero}}(k)$$

$$\text{FT}(I_{\text{act}}(x)) = J_{\text{act}}(k)$$

Here,  $k$  is the spatial frequency in increments of  $1/(2 \cdot d_{\text{pix}} \cdot N_x)$  [ $\text{m}^{-1}$ ].

We know that  $I_{\text{act}}(x)$  is (in theory) a shifted copy of  $I_{\text{zero}}(x)$ . The shift is equal to the wafer height change ( $dZ_{\text{waf}}$ ) times a proportionality factor  $\gamma$ :

$$I_{\text{act}}(x) = I_{\text{zero}}(x - \gamma \cdot dZ_{\text{waf}})$$



Fringe patterns after normalisation. The horizontal axis represents  $x$ -position on the CMOS-sensor, as unit pixels. The vertical axis represents irradiance, normalised as explained in the text. The shape of the two fringe patterns is (approximately) the same. The 'blocky' signal at the edges is a result of highly amplified noise.

- (a) Zero measurement.
- (b) Actual measurement.

The nominal value of  $\gamma$  is known, as it follows from sensor hardware parameters (angle of incidence at wafer, angle of interference, wavelength, magnification of lens set, pixel spacing). This nominal value  $\gamma$  is used in further calculations.

The relation between the two Fourier transforms is [6]:

$$J_{act}(k) = J_{zero}(k) \cdot (-i \cdot k \cdot \gamma \cdot dZ_{waf})$$

Multiplying  $J_{act}(k)$  by the complex-conjugate of  $J_{zero}(k)$  yields:

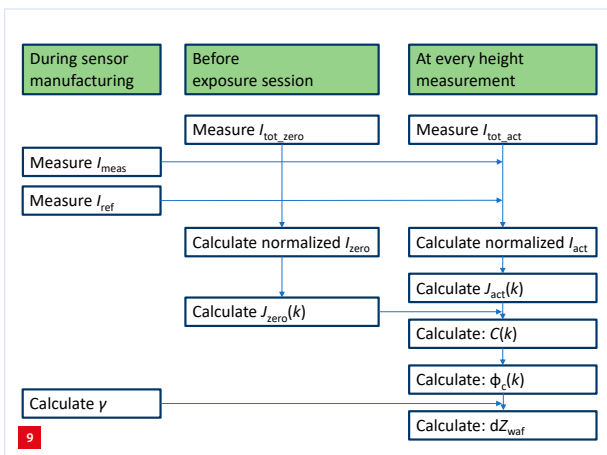
$$C(k) = \overline{J_{zero}(k)} \cdot J_{act}(k) = \overline{J_{zero}(k)} \cdot J_{zero}(k) \cdot \exp(-i \cdot k \cdot \gamma \cdot dZ_{waf})$$

or

$$C(k) = |J_{zero}(k)|^2 \cdot \exp(-i \cdot k \cdot \gamma \cdot dZ_{waf})$$

Note the term  $|J_{zero}(k)|^2$  is real and that therefore the information of interest ( $dZ_{waf}$ ) has a very simple and direct relation with the phase of  $C(k)$  (i.e.  $\phi_c(k)$ ). That relation is:

$$\phi_c(k) = -k \cdot \gamma \cdot dZ_{waf}$$



Data-processing steps.

The phase of  $C(k)$  can be calculated using an arctan-function. The slope in  $k$ -space ( $-\gamma \cdot dZ_{waf}$ ) can be found using a line fit in a  $k$ - $\phi_c$ -plot. Division by  $-\gamma$  then yields the estimated wafer height change  $dZ_{waf}$ .

The above-described process is shown graphically in Figure 9. Although this appears straightforward, there are unfortunately a few difficulties. The first difficulty is that when the phase data  $\phi_c(k)$  is calculated using an atan2-function [7], the resulting data is wrapped modulo  $2\pi$ . This can be solved with unwrapping algorithms (which are readily available or can be self-written).

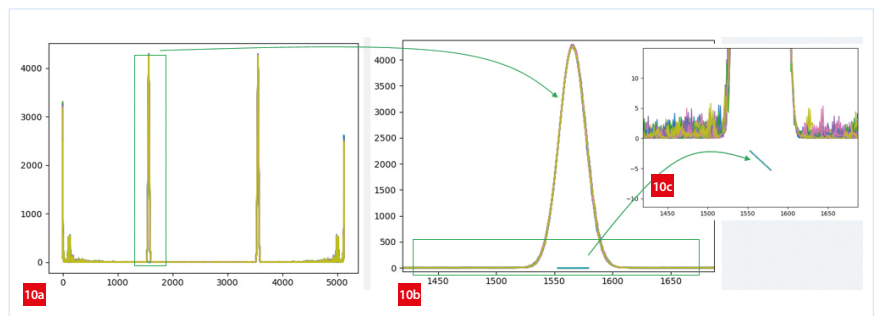
A second, more severe issue is that  $C(k)$  only contains useful (non-zero) data within the peak at the spatial frequency of the fringes; see Figure 10. At most other spatial frequencies,  $C(k)$  is nearly zero and calculation of  $\phi_c(k)$  yields useless data when using:

$$\phi_c(k) = \text{atan2}(\text{real}(C(k)), \text{imag}(C(k)))$$

It is possible to evaluate data within the peak and a correct line fit can be done, but the accuracy of this line fit is poor because the  $k$ -extent of the peak is small.

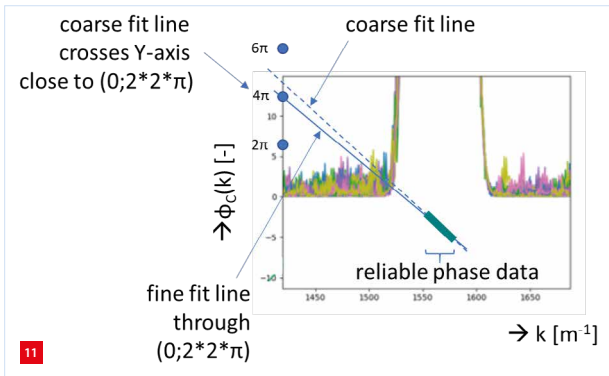
The phase relation predicted by theory ( $\phi_c(k) = -k \cdot \gamma \cdot dZ_{waf}$ ) implies that points  $(k, \phi_c(k))$  lie on a line that passes through the origin. Snapping the line fit to the origin would improve the accuracy of the line fit, because the origin is relatively far away. The problem is that – at the peak – merely  $\phi_c(k) + 2\pi N$  is available, where  $N$  is an unknown integer. So, extending the line fit leftwards will generally not intersect the  $y$ -axis at the origin, but at a point  $(0, 2\pi N)$ , where  $N$  can be any integer.

Fortunately, it turns out – for the realised sensor – that the coarse, leftwards extrapolation always intersects sufficiently closely to the correct 'y-axis-intersection point'. We therefore let the line fit snap to the  $(0, 2\pi N)$ -point that is closest to the



Irradiance plots. The horizontal axes represent spatial frequency: unit is  $1/(2 \cdot d_{pix} \cdot N_x)$ , where  $d_{pix}$  is the pixel spacing and  $N_x$  is the number of horizontal pixels, 2,560. The vertical axes represent irradiance amplitude in arbitrary units, respectively phase (for the upper right green/cyan plot); unit is radians.

- (a)  $|C(k)|$ .
- (b) Horizontal zoom-in (at the spatial frequency of the fringes) of  $|C(k)|$  and  $\phi_c(k)$ , which can be seen in green/cyan below the central irradiance peak.
- (c) Vertical zoom-in of the phase data  $\phi_c(k)$ .



Coarse and fine line fit to phase-spatial frequency data.

intersection of the coarse line fit and the  $y$ -axis (Figure 11). Then, using a least-squares criterion, we fit the line to the  $\phi_C(k)$ -points that lie within the peak. The result is a line that passes through one point of the series  $(0, 2\pi N)$  and as close as possible to the points  $\phi_C(k)$ . This yields a 'fine' estimate of the line slope, which is subsequently divided by  $\gamma$  to yield the estimated wafer height change ( $\bar{\Delta z}_{waf}$ ).

### Assembly

The review process in the system design led to a high-quality mechanical design and no surprises were found in the assembly of the sensor (Figure 12). The adjustable folding mirrors were locked in their kinematic mounts using adhesive. The rest (parts and sub-assemblies) was mounted and locked using locking screws. *OPL* alignment ensured that fringes were formed in the centre of the detector when the wafer was at the centre of the sensor's vertical measurement range.

To enable sensor testing (with respect to functionality and stability), a dedicated frame and a stationary wafer, mounted on a wafer table, were added, as shown in Figure 13. A statically determined mounting with ceramic balls and V-grooves was used to position the frame holding the sensors with respect to the frame holding the wafer table.



Assembly of the sensor.  
(a) Inside the flowbench.  
(b) Optical fibre inside ring module.  
(c) Ring module shown upside down.

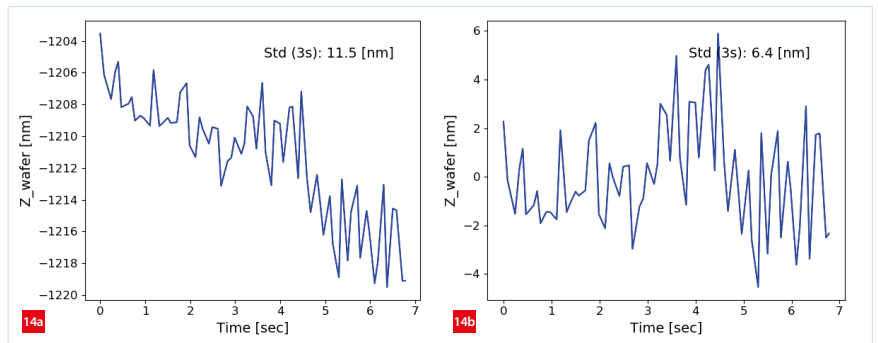


Assembled sensor. The sensor ring (aluminium colour) is suspended from the top frame (blue), which stands on the bottom frame (blue), which in turn carries a 300-mm wafer (only the edge visible on the left).  
(a) Rendering.  
(b) Realisation.

Height measurements were performed at one point in the centre of the wafer, as there was no  $xy$ -stage.

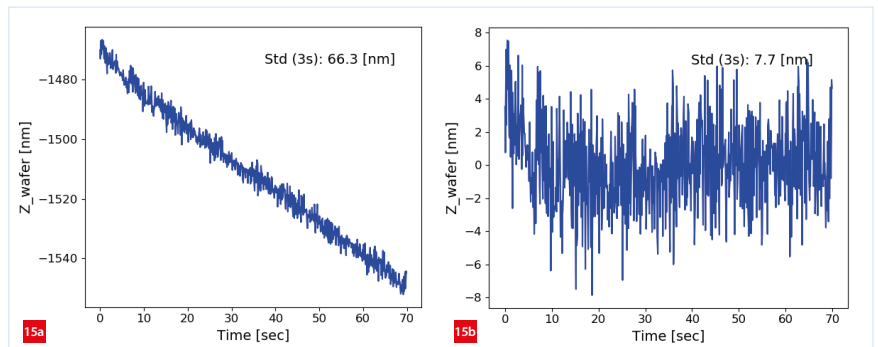
### Testing

At our production facility, stability tests were executed inside a flowbench. During various time durations, ranging from 1 to 300 seconds, frames were recorded onto a PC hard drive. This data was analysed offline using the previously described data-processing algorithms. Time scales in the order of seconds or even a few minutes would correspond to the time a wafer spends in a lithography tool for one exposure. When recording seventy frames in 7 seconds, the observed stability ( $3\sigma$  standard deviation, std) was 11.5 nm, and 6.4 nm after a linear detrend of the data; see Figure 14.



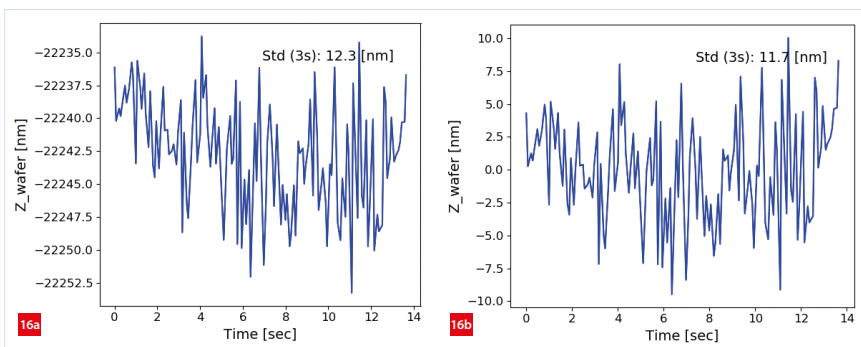
Wafer height measurement during 7 seconds.  
(a) Raw data.

(b) Data after linear detrend.

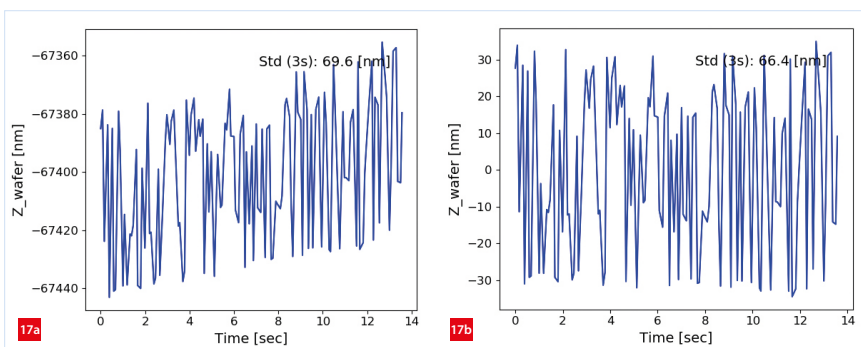


Wafer height measurement during 70 seconds.  
(a) Raw data.

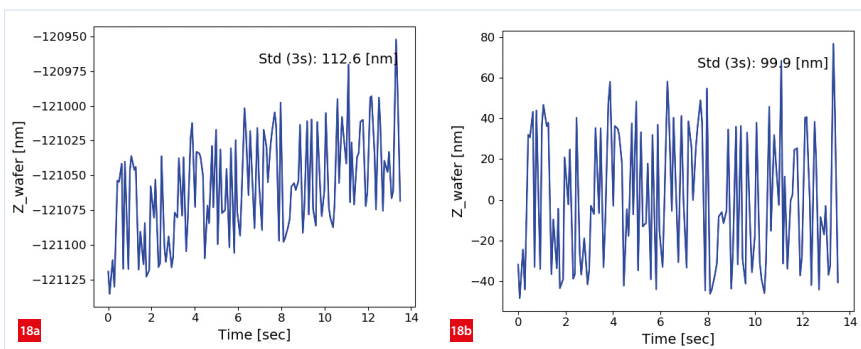
(b) Data after linear detrend.



Wafer height measurement with the wafer effectively lowered by about 20  $\mu\text{m}$ .  
 (a) Raw data. (b) Data after linear detrend.



Wafer height measurement with the wafer effectively lowered by about 60  $\mu\text{m}$ .  
 (a) Raw data. (b) Data after linear detrend.



Wafer height measurement with the wafer effectively lowered by about 120  $\mu\text{m}$ .  
 (a) Raw data. (b) Data after linear detrend.

Note: in Figures 14 to 18, Std (3s) denotes Std ( $3\sigma$ ). It is not known precisely whether the linear trend originates from the sensor or from the environment (frame or wafer table). A longer measurement (700 frames during 70 seconds) revealed a comparable result (Figure 15). The raw height measurement contained a clear trend/drift, which led to an observed instability ( $3\sigma$  std) of 66.3 nm. The instability after linear detrend was a mere 7.7 nm.

Tests were also conducted to check whether the required measurement range (300  $\mu\text{m}$  peak-to-peak) was reached. The wafer was lowered virtually by raising the sensor ring by placing shim plates between the top and bottom frames. In a first test, the ring was raised by about 20  $\mu\text{m}$ . This resulted in an observed instability of 12.3 nm ( $3\sigma$  std); see Figure 16. As there was no linear trend/drift, the instability of the detrended data was about equal.

In a second test, the ring was raised by about 60  $\mu\text{m}$  (compared to the case without shims). The observed instability was 69.6 nm ( $3\sigma$  std); see Figure 17. As there was only a small linear trend/drift, the observed instability of the detrended data was about equal.

In a third test, the ring was raised by about 120  $\mu\text{m}$  (compared to the case without shims). The observed instability was 112.6 nm ( $3\sigma$  std); see Figure 18. The observed instability of the detrended data was 99.9 nm.

## Conclusions and outlook

The test results show that the short-term (linearly detrended) instability of the sensor can be as low as 7.7 nm. This is a very satisfying result when compared to the maximum permitted instability of 50 nm. It also became clear that during longer measurement sequences (70 seconds), the observed drift can be as large as 60 nm per minute. It is not currently known whether this behaviour originates from the sensor ring or from its environment (frame + wafer). The next stage of research will focus on bringing stability performance within specification throughout the 300  $\mu\text{m}$  range.

In this respect, it is also relevant to clarify how the stability of the environmental temperature in the executed tests relates to the stability of the temperature inside a semiconductor lithography tool (which is generally very tightly controlled). To that end, sensor drift will be measured in an environment with improved temperature stability (< 20 mK). Depending on our findings, we will decide whether to invest in a thermo-mechanical redesign of the sensor. Finally, the test results show that the short-term stability of the sensor increases significantly when the wafer height difference (between zero measurement and actual measurement) increases. The cause of this effect is not currently understood. We will invest in understanding this behaviour, because the largest observed short-term instability (99.9 nm) significantly exceeds the maximum permitted instability of 50 nm.

Further research will explore the simultaneous measurement of wafer height as well as wafer tip/tilt ( $R_x$  and  $R_y$ ) by also measuring the angle of the interference pattern on the camera and the pitch of the fringes in the interference pattern. The tip/tilt parameters relate linearly to the fringe spacing and fringe orientation on the detector, which can both be extracted from the recorded 2D image. Applications can benefit from this additional functionality, for example in counteracting tilt-dependent wafer height measurement errors (e.g. Abbe errors).

## REFERENCES

- [1] [www.mitutoyo.co.jp/eng//useful/E11003/pdf/48.pdf](http://www.mitutoyo.co.jp/eng//useful/E11003/pdf/48.pdf)
- [2] [www.micro-epsilon.com](http://www.micro-epsilon.com)
- [3] [www.superlumdiodes.com/sld-mcs-scs-series.htm](http://www.superlumdiodes.com/sld-mcs-scs-series.htm)
- [4] [en.ids-imaging.com/store/products/cameras/ui-3482le.html](http://en.ids-imaging.com/store/products/cameras/ui-3482le.html)
- [5] [en.wikipedia.org/wiki/Nyquist-Shannon\\_sampling\\_theorem](http://en.wikipedia.org/wiki/Nyquist-Shannon_sampling_theorem)
- [6] [en.wikipedia.org/wiki/Fourier\\_transform](http://en.wikipedia.org/wiki/Fourier_transform)
- [7] [www.scipy.org](http://www.scipy.org)